

# Microstructures and Stabilization Mechanisms of Nanocrystalline Iron-Chromium Alloys with Hafnium Addition



WEIZONG XU, LULU LI, MOSTAFA SABER, CARL C. KOCH, YUNTIAN ZHU,  
and RONALD O. SCATTERGOOD

The low thermal stability of nanocrystalline metals severely limits their applications at high temperatures. In this study, we investigate the nanocrystalline stabilization mechanisms for Fe-14Cr alloys with 1, 2, and 4 at. pct Hf addition at 1173 K (900 °C). Microstructural characterizations using aberration-corrected scanning transmission electron microscopy and energy-dispersive X-ray spectroscopy reveal high density of HfO<sub>2</sub> nanoparticles with sizes of ~4 nm dispersed throughout the ferritic matrix. This indicates that kinetic stabilization by HfO<sub>2</sub> nanoparticle pinning is primarily responsible for the observed high thermal stability. In addition, some Hf and Cr segregation on grain boundaries is observed in the Fe-14Cr-4Hf, suggesting the existence of thermodynamic stabilization at high Hf content. Second-phase precipitations such as hafnium carbide, M<sub>23</sub>C<sub>6</sub>, and Fe-Cr-Hf intermetallic phase are also found in the Fe-14Cr-4Hf, but their large sizes and inter-spacing suggest that their contribution to stabilization is minimal.

DOI: 10.1007/s11661-015-2985-2

© The Minerals, Metals & Materials Society and ASM International 2015

## I. INTRODUCTION

NANOCRYSTALLINE materials, with grain sizes less than 100 nm, have attracted extensive attention due to their unique physical, chemical, electrical, and mechanical properties.<sup>[1–6]</sup> These enhanced properties are intrinsically related to large grain boundary area per unit volume in nanocrystalline materials. Nevertheless, a large grain boundary area per unit volume makes nanocrystalline materials thermally unstable and susceptible to grain coarsening to reduce the total grain boundary energy. The low thermal stability of nanocrystalline materials is a roadblock to many applications, especially at elevated temperatures. It has been reported that substantial grain growth can occur even at room temperature in nanocrystalline Cu,<sup>[7]</sup> Al,<sup>[8]</sup> and Ag.<sup>[9]</sup> The understanding of the thermal stability mechanisms in nanocrystalline materials is fundamentally needed to design thermally stable nanocrystalline materials for applications at elevated temperatures.

In the last decade, significant improvements in the thermal stability of nanocrystalline materials have been reported.<sup>[10–17]</sup> Most of them are multicomponent systems, either alloys or containing second-phases and/or impurities. Mechanisms that can stabilize nanocrystalline materials include solute drag, second-phase-particle pinning (also called Zener pinning), lowering

grain boundary energy by segregation of solute atoms (thermodynamic stabilization), chemical ordering, and porosity.<sup>[13]</sup> At high temperatures, Zener pinning or thermodynamic stabilization is believed to play a dominant role in grain stabilization. The former is a kinetic stabilization by second-phase particles that can be described by the Zener equation.<sup>[18]</sup> This mechanism has been found to contribute to the superior stability of nanocrystalline Al and Fe-Al alloys,<sup>[15,16]</sup> in which the small size and large volume fraction of particles produce pinning. The thermodynamic stabilization mechanism, on the other hand, utilizes the grain boundary segregation of non-equilibrium solute atoms to produce a minimum in the Gibbs excess free energy of grain boundaries, and consequently suppresses grain coarsening.<sup>[19–21]</sup> This mechanism was found responsible for the high thermal stability of nanocrystalline Ti-W or Al-Pb alloys, in which no precipitation of second-phase particle was observed.<sup>[19,20]</sup> As a matter of fact, in many alloy systems such as Fe-Zr,<sup>[11,12]</sup> Fe-Cr-Zr,<sup>[10,22]</sup> Ni-Mn,<sup>[23]</sup> Co-P,<sup>[24]</sup> or Ni-P,<sup>[25,26]</sup> both second-phase precipitation and grain boundary segregation could occur and compete for solute atoms from the matrix.

In a recent work, our group reported that Hf could help stabilize nanocrystalline Fe-Cr alloys at temperatures up to 1273 K (1000 °C), in which both particle pinning and Hf grain boundary segregation were proposed as the stabilization mechanisms.<sup>[27]</sup> Two important issues are still not well understood. (1) Among the different kinds of second-phases existing in the microstructure, which second-phase is primarily responsible for the particle pinning effect? (2) Thermodynamic stabilization by the segregation of alloy elements to the grain boundaries has been proposed by theoretical

WEIZONG XU and MOSTAFA SABER, Postdoc Scholars, LULU LI, Graduate Student, CARL C. KOCH, YUNTIAN ZHU, and RONALD O. SCATTERGOOD, Professors, are with the Department of Materials Science and Engineering, North Carolina State University, Raleigh, NC 27695. Contact e-mail: ytzhu@ncsu.edu  
Manuscript submitted October 2, 2014.

Article published online June 2, 2015

modeling, but direct experimental evidences are still lacking.

This raises another fundamental question: which mechanism plays a dominant role when both particle pinning and grain boundary segregation co-exist and compete for solute atoms from the matrix?<sup>[28]</sup> More study is therefore needed to help clarify this issue. This requires a comprehensive characterization of the distribution of second-phase particles and grain boundary segregation in both nano-scale and a large field of view. However, such an observation turns out to be difficult using conventional TEM or atom probe tomography (APT).<sup>[29,30]</sup>

Fast and comprehensive microstructure investigation can be realized by employing aberration-corrected scanning transmission electron microscopy (STEM) equipped with Super-X™ energy-dispersive X-ray spectroscopy (EDS) system. The contrast of the high-angle annular dark-field (HAADF) STEM image is proportional to the average atomic number ( $Z$ ) and the material density,<sup>[31]</sup> which makes it possible to clearly distinguish different types of second-phase particles in the microstructure. This technique enables us to detect all particles in the observed area, making particle distribution analysis more reliable. It largely overcomes the experimental difficulty in detecting all of the particles using conventional TEM. In addition, the newly developed Super-X™ EDS system is equipped with four large-area silicon drift detectors (SDD) and a much larger collection solid angle (0.7 sr) for EDS signal detection.<sup>[32]</sup> It not only allows a fast elemental mapping over large areas to determine phase chemistry but also enables us to resolve the solute elements at low concentration levels and in high spatial resolutions.<sup>[30]</sup> The utilization of the HAADF-STEM and the Super-X™ EDS system allows us to characterize second-phase particles and solute segregation at grain boundaries with unprecedented information, providing more reliable experimental results for thermal stability mechanism study in nanocrystalline materials.

In this paper, we present the direct observation of stabilization mechanisms in nanocrystalline Fe-14Cr alloys with systematic variation of the Hf addition using aberration-corrected STEM and the Super-X™ EDS, including (1) accurate measurement of the different second-phase precipitations in the alloy, (2) experimental evidence of grain boundary segregation. The existence and the competition between Zener pinning and thermodynamic stabilization mechanisms are revealed. Fe-14Cr- $x$ Hf alloys are selected as model materials, since Hf has a much larger atomic number ( $Z = 72$ ) than Fe ( $Z = 26$ ) or Cr ( $Z = 24$ ) species in the alloy, making it much easier to detect both Hf precipitation and segregation in STEM. In addition, the effect of Zr is expected to be similar to Hf, due to their similar chemical properties, in stabilizing the Fe-Cr alloy.<sup>[10,33]</sup> Therefore, the findings in this study could also provide relevant and useful information for Fe-Cr alloys stabilized by other elements such as Zr.

## II. EXPERIMENTAL PROCEDURE

Fe-14Cr- $x$ Hf alloys with  $x$  equals 1, 2, and 4 at. pct were synthesized by mechanical alloying in a SPEX 8000M Mixer/Mill. Fe, Cr, and Hf powders from Alfa Aesar, with 99.9, 99.9, and 99.6 pct purity, respectively, were used as starting materials. They were mixed under Ar atmosphere, and then milled with stainless steel balls in a hardened steel vial for 20 hours. The ball to powder mass ratio was 10:1. X-ray diffraction analysis revealed that the milling produced non-equilibrium solid solutions.<sup>[27]</sup> The as-milled powders were subsequently annealed at 1173 K (900 °C) for 1 hour under Ar-2 pct H<sub>2</sub> protective atmosphere.

Scanning/transmission electron microscopy (S/TEM) samples were prepared using the focused ion beam (FIB) 'lift-out' technique in an FEI Quanta 3D FEG dual-beam instrument. The FIB specimen was directly cut from the annealed powder agglomerates, and then milled by Ga<sup>+</sup> ions at 30 kV, followed by final thinning and polishing at 5 and 2 kV.

HAADF-STEM images were taken in an aberration-corrected FEI Titan G2 microscope operated at 200 kV. The probe size, convergence angle, and collection inner semi-angle were 0.1 nm, 21 mrad, and 77 mrad, respectively. STEM imaging simulation was performed by the QSTEM package,<sup>[34]</sup> using same microscope configuration for the calculation.

EDS elemental mapping was also acquired in the Titan G2 microscope. The acquisition rates for EDS signal were ~1.0 to 2.0 kcps, which varied with samples. Five sets of EDS mapping were taken for the sample: (1) 232 × 232 pixels over an area of 11 × 11 nm for 600 seconds, (2) 344 × 396 pixels over an area of 63 × 73 nm for 3600 seconds, (3) 184 × 160 pixels over an area of 48 × 42 nm for 270 seconds, (4) 356 × 332 pixels over an area of 186 × 174 nm for 900 seconds, (5) 368 × 368 pixels over an area of 535 × 535 nm for 900 seconds. EDS composition analysis was conducted using the Cliff-Lorimer method in Bruker Esprit software.

Conventional TEM images were taken in a JEM-2010F microscope operated at 200 kV. The electron diffraction patterns of the given crystal structure were simulated using the JEMS software.<sup>[35]</sup>

## III. RESULTS

The Hf concentration significantly affects the microstructures. Figures 1(a) through (c) are TEM images of the microstructures of the Fe-14Cr- $x$ Hf alloys after annealing at 1173 K (900 °C) for 1 hour, where  $x$  is 1, 2, and 4 at. pct, respectively. Figure 1(a) shows that the Fe-14Cr-1Hf alloy exhibits a bimodal grain size distribution, which contains both 1 to 5 μm micro-size grains and 100 to 300 nm ultrafine grains. Some ultrafine grains appear to be elongated in shape. By increasing the Hf concentration to 2 and 4 at. pct, the nanocrystalline microstructure is stabilized after annealing. It contains equiaxed grains with average grain size of 66 nm for the

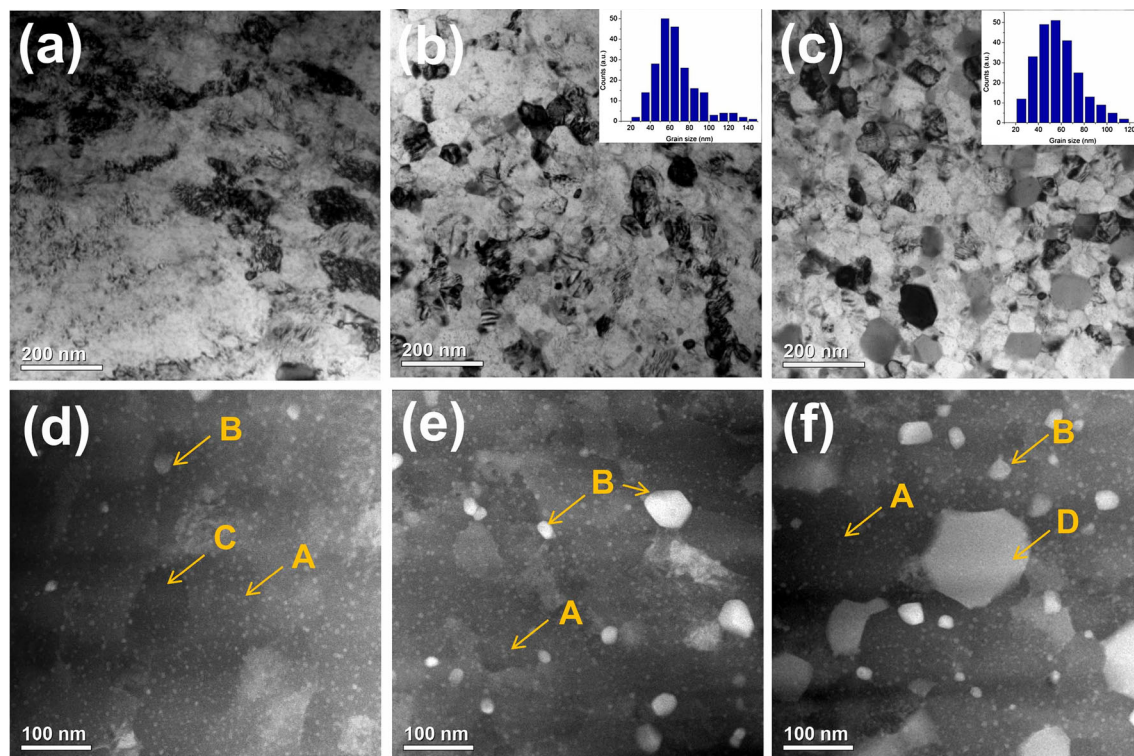


Fig. 1—Microstructure of the Fe-14Cr- $x$ Hf alloy after annealing for 1 hour at 1173 K (900 °C). TEM images for  $x$  equals to (a) 1 at. pct Hf, (b) 2 at. pct Hf, (c) 4 at. pct Hf. HAADF-STEM images for  $x$  equals to (d) 1 at. pct Hf, (e) 2 at. pct Hf, (f) 4 at. pct Hf. Histograms of grain size distribution of Fe-14Cr-2Hf and Fe-14Cr-4Hf are shown on the right-top corner of (b) and (c), respectively. For the Fe-14Cr-1Hf alloy, histogram is not shown due to fact that the alloy exhibits the bimodal grain size distribution and some ultrafine grains appear to be elongated in shape.

Fe-14Cr-2Hf alloy (Figure 1(b)) and 57 nm for the Fe-14Cr-4Hf alloy (Figure 1(c)). The annealing temperature of 1173 K (900 °C) is  $\sim 0.66 T_m$  of the Fe-14Cr-based alloy. At such a high homologous temperature, most nanocrystalline materials are expected to be unstable and to undergo rapid grain growth. This is also seen from the observation that the nanocrystalline Fe-14Cr alloy without Hf additions is coarsened to about 5 to 10  $\mu\text{m}$  grain size after 1173 K (900 °C) annealing for 1 hour. The fact that the Fe-14Cr-2Hf and Fe-14Cr-4Hf alloys still retained their nanocrystalline structures after being annealed at 1173 K (900 °C) demonstrates their good thermal stability.

HAADF-STEM images of these alloys are shown in Figures 1(d) through (f). It is found that there exists some additional phases in the microstructure other than the existing ferritic matrix (dark contrast in the background). One common feature of the annealed alloys is the presence of dot-like particles with bright contrast [marked as A in Figures 1(d) through (f)], which suggests the formation of nano-size particles in the microstructure after annealing at 1173 K (900 °C). Other particles labeled as B, C, and D are also seen in Figure 1, and will be discussed in a later section. As seen in Figure 2(a), these A particles are nearly spherical in shape and uniformly dispersed throughout the ferritic grains. The sizes of these particles are in the range of 1 to 10 nm, as shown by the histograms in Figure 3. The average particle size slightly drops from 4.3 and

3.7 nm, as the Hf concentration increases from 1, to 2 and 4 at. pct, respectively. More importantly, a number of nano-size particles are found at grain boundaries (marked as yellow dash lines) in Figure 2(a). The grain boundary segment near the particle becomes uneven, as shown Figure 2(b). This suggests that these nano-size particles are effectively pinning the grain boundaries to retard grain growth. Figure 2(c) shows a nano-size particle in the grain interior is the pinning dislocation. Note that both the particles formed at the grain boundary (in Figure 2(b)) and in the grain interior (in Figure 2(c)) appear to have lattice fringes in the high-resolution HAADF-STEM images, suggesting a certain type of crystalline structure for these nano-size particles.

Energy dispersive X-ray spectroscopy (EDS) elemental mapping technology is employed to further investigate the chemical composition of the nano-size particles. Figure 4(a) shows typical EDS mapping results from a region in the Fe-14Cr-2Hf alloy. Hf and O are found in the EDS mapping area of nano-size particle A, while Fe and Cr are depleted, suggesting that the particles are most likely to be  $\text{HfO}_2$ . Similar results are also found from the other two alloys with different Hf contents (*i.e.*, 1 at. pct Hf and 4 at. pct Hf).

The formation of  $\text{HfO}_2$  is confirmed by the electron diffraction analysis. Figure 4(b) shows the selected area electron diffraction pattern (SAED) taken in a region that contains both the ferritic matrix and the nano-size particles in the Fe-14Cr-1Hf sample. Additional

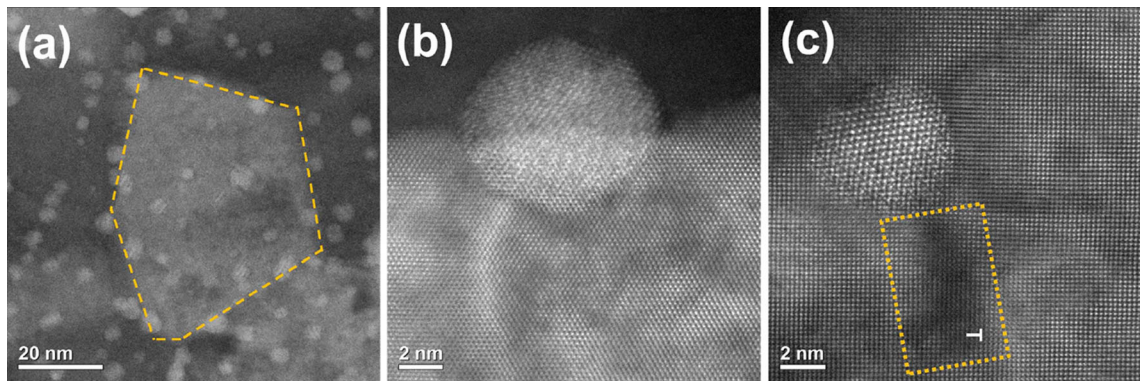


Fig. 2—HAADF-STEM images of nano-size particles in the Fe-14Cr-2Hf alloy. (a) Some of particles are pinned at the grain boundaries (which are marked as yellow dash lines). The atomic resolution images of one particle located (b) at the grain boundary and (c) inside the ferritic grain are obtained. The distort region in (c) is drawn by a rectangular with yellow dash lines which includes a dislocation inside it (Color figure online).

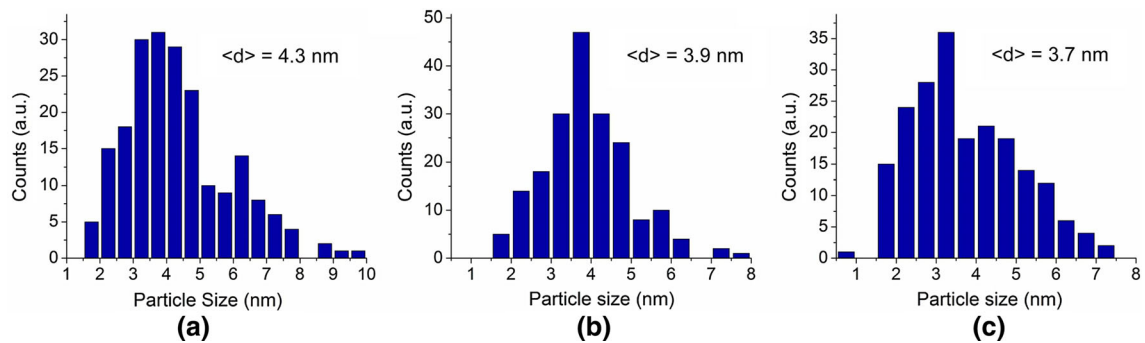


Fig. 3—Particle size histograms of the nano-size phase (particle A) in the Fe-14Cr- $x$ Hf alloy where  $x$  equals to (a) 1 at. pct Hf, (b) 2 at. pct Hf, (c) 4 at. pct Hf. The average particle sizes are 4.3, 3.9, and 3.7 nm, respectively.

diffraction rings (marked by red circles) are found in Figure 4(b), along with the rings from the body centered cubic (bcc) ferritic matrix (marked by blue circles). Dark-field TEM images taken from these additional diffraction rings show that the dot-like particle contrast (in Supplementary Figure S1) has similar morphology to that of the nano-size Hf- and O-enriched particles, implying that these diffraction rings are from these particles. Diffraction intensity (shown as light blue peaks in Figure 4(b)) is further integrated as a function of the ring diameter ( $\text{nm}^{-1}$ ) in order to quantitatively determine the position of the diffraction rings. Such peaks are further compared in Figure 4(c) with the simulated electron diffraction peaks of (i) the bcc matrix, (ii) three existing crystal structures of  $\text{HfO}_2$ , *i.e.*, orthorhombic  $\text{HfO}_2$  (Pbca<sup>[36]</sup>), tetragonal  $\text{HfO}_2$  (P 42/nmc<sup>[37]</sup>), and monoclinic  $\text{HfO}_2$  (P 21/c<sup>[38]</sup>). The positions of the diffraction peaks are found to best match those of the orthorhombic  $\text{HfO}_2$ . It should be noted that the positions of the  $\text{HfO}_2$  diffraction rings are similar in all three Fe-14Cr- $x$ Hf alloys (see Supplementary Figure S2). Here, we specifically choose the Fe-14Cr-1Hf alloy for the diffraction analysis. This is due to the fact that for Fe-14Cr-2Hf and Fe-14Cr-4Hf alloys, SAED patterns also contain additional electron diffraction spots from other second-phases, some of which could overlap with the  $\text{HfO}_2$  peak.

The observed orthorhombic  $\text{HfO}_2$  phase is known to be a high pressure phase rather than the monoclinic

phase formed at ambient condition.<sup>[39]</sup> It is possible that the nanoparticle size or the ferritic matrix constraint might have helped stabilize the orthorhombic crystal structure.<sup>[40–43]</sup> Such orthorhombic  $\text{HfO}_2$  phase is also reported in high- $k$  dielectric  $\text{HfO}_2$  films deposited on a Si/SiO<sub>2</sub> substrate by atomic layer deposition (ALD) and pulsed laser deposition (PLD).<sup>[44]</sup>

Figure 5 shows the HAADF-STEM image and EDS mapping of a grain boundary area in the Fe-14Cr-4Hf alloy. The bright dot-like particles are  $\text{HfO}_2$  uniformly distributed in the matrix. Interestingly, two bright grain boundary segments are detected in Figure 5(a), as marked by the yellow arrows. EDS mapping of this area further reveals that the bright grain boundaries are rich in Hf and Cr. Such a Hf and Cr co-segregation has also been observed in other grain boundary areas with similar bright-line contrast (see Supplementary Figure S3). As the model predicted, the Hf segregation to the grain boundary is expected to produce a minimum in the grain boundary Gibbs excess free energy, which reduces the thermodynamic driving force for grain growth.<sup>[19–21]</sup> It should be noted that the bright-line grain boundary contrast in Figure 5(a) should have mostly come from Hf, because the atomic number of Hf is much larger than that of Fe or Cr. This bright-line feature provides a convenient way to investigate Hf segregation in the microstructure. As shown in Figure 6(a), these bright lines of Hf and Cr co-segregation occur in a small

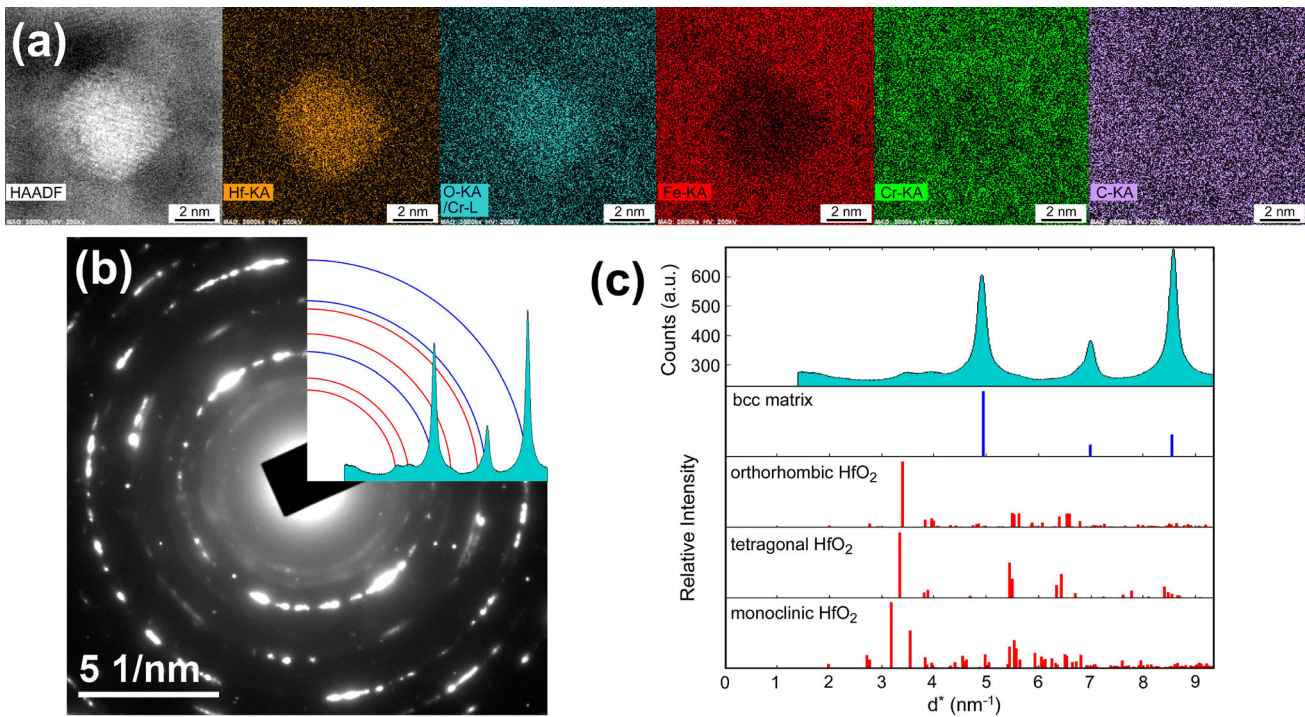


Fig. 4—Chemical and crystal structure analysis of the nano-size particles. (a) Energy dispersive X-ray spectroscopy (EDS) mapping of the particle in the Fe-14Cr-2Hf alloy, which includes the HAADF-STEM image and the elemental mapping of the Hf, O, Fe, Cr species. (b) Selected area diffraction pattern of a region contains both the body centered cubic (bcc) ferritic matrix and nano-size particles in the Fe-14Cr-1Hf alloy. (c) Simulated electron diffraction patterns of HfO<sub>2</sub> in orthorhombic, tetragonal, and monoclinic crystal structure (red lines) and bcc ferritic matrix (blue lines) as a function of the plane spacing in reciprocal space (nm<sup>-1</sup>) (Color figure online).

fraction of grain boundaries in a typical region of the Fe-14Cr-4Hf alloy. It is also found that some grain boundaries segments have heavy co-segregation, as shown in Figure 6(b). However, such solute grain boundary segregation has not been detected in Fe-14Cr-1Hf or Fe-14Cr-2Hf alloys, suggesting that the segregation of Hf and Cr to grain boundaries only occurs when the Hf content is higher than a critical value.

The phase with the brightest contrast in the HAADF-STEM images is labeled as B in Figures 1(d) through (f). According to EDS mapping in Figure 7(a), it is enriched with Hf and C, and depleted of Fe and Cr, suggesting a hafnium carbide phase. This phase has a face-centered cubic (fcc) structure,<sup>[45]</sup> which is consistent with the atomic resolution STEM observations along various crystallographic orientations as shown in Figures 7(b) through (d). The average size of the hafnium carbide phase is estimated to be 19, 23, and 20 nm for the 1, 2, and 4 at. pct Hf, respectively. And the volume fraction of hafnium carbide in Fe-14Cr-1Hf appears to be much less than that in Fe-14Cr-2Hf or in Fe-14Cr-4Hf alloys (see Figures 1(d) through (f)).

The large particle labeled as C in Figure 1(d) is identified as another carbide phase. These particles have sizes in the range of 50 to 150 nm and a slightly darker contrast in the HAADF-STEM image, as shown in Figures 1(d) or 8(a). EDS elemental mapping reveals that they are enriched with Cr and C and contains some Fe, with a Cr to Fe atomic ratio of about 1.8:1. Atomic-

resolution HAADF-STEM images are obtained along the [112] orientation (Figure 8(b)) and the [102] orientation (Figure 8(c)). Both agree well with the simulated HAADF images of the M<sub>23</sub>C<sub>6</sub> phase (Fm-3 m<sup>[46]</sup>), where M stands for Fe or Cr. The corresponding projections of the atoms column are illustrated on their right side. These results suggest that this is an M<sub>23</sub>C<sub>6</sub> phase with a chemical composition close to (Cr<sub>0.64</sub>Fe<sub>0.36</sub>)<sub>23</sub>C<sub>6</sub>. Interestingly, this carbide phase is observed in the Fe-14Cr-1Hf alloy, but not in the other two alloys with higher Hf concentrations.

The major microstructural difference between the Fe-14Cr-2Hf and the Fe-14Cr-4Hf alloys after the 1173 K (900 °C) annealing is the existence of an additional phase in the Fe-14Cr-4Hf alloy, labeled as D in Figure 1(f), which is typically large (~40 to 140 nm) with bright contrast in the HAADF-STEM image. EDS elemental mapping is performed to identify this phase, as marked by yellow arrows in Figure 9, which reveals an atomic ratio of Fe to Cr to Hf as about 1:0.08:0.33. This ratio is close to (Fe, Cr)<sub>3.3</sub>Hf, which is different from other reported intermetallic phases such as Fe<sub>2</sub>Hf or Cr<sub>2</sub>Hf phases.<sup>[47,48]</sup> Some intermetallic phases such as Fe<sub>3</sub>Zr and Fe<sub>23</sub>Zr<sub>6</sub> were reported in Fe-Zr alloys,<sup>[49,50]</sup> but their counterparts were not observed in Fe-Hf or Fe-Cr-Hf alloy systems. The exact crystal structure of this new intermetallic phase in the Fe-Cr-Hf alloy is still unclear and needs to be further investigated.

Table I summarizes the phases observed in the Fe-14Cr-xHf alloys and their sizes after 1173 K (900 °C)

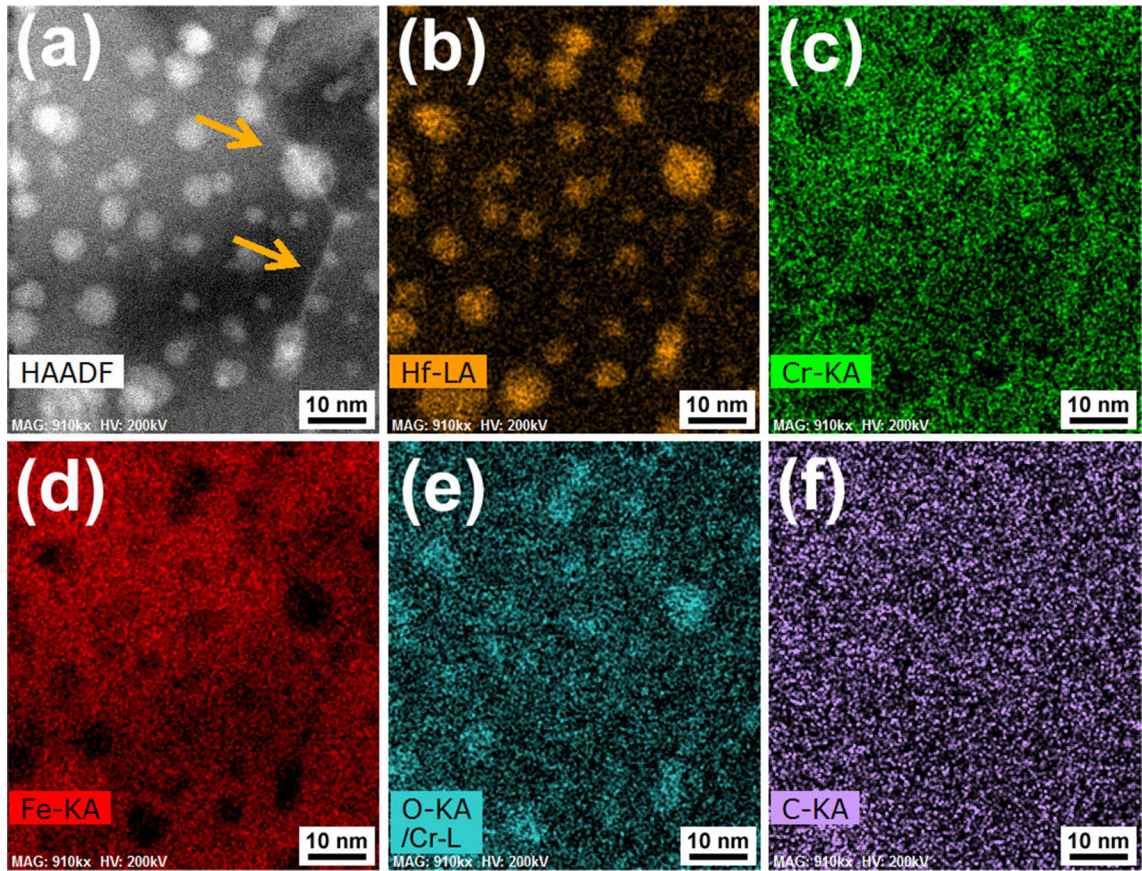


Fig. 5—EDS elemental mapping of an area near the grain boundary in the Fe-14Cr-4Hf alloy. (a) HAADF-STEM image. Elemental mapping of (b) Hf-L $\alpha$ , (c) Cr-K $\alpha$ , (d) Fe-K $\alpha$ , and (e) O-K $\alpha$ /Cr-L (f) C-L $\alpha$ . As marked by the yellow arrows in (a), bright lines appear at grain boundaries in the HAADF-STEM image, which corresponds to Hf and Cr segregation in these areas (Color figure online).

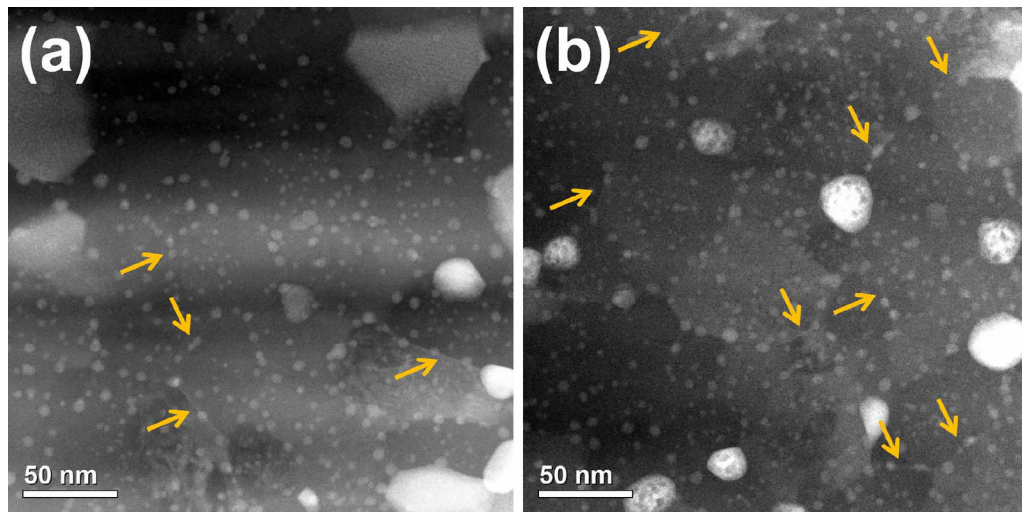


Fig. 6—HAADF-STEM images of the Fe-14Cr-4Hf alloy. Hf and Cr grain boundary segregation has been shown as bright line features pointed out by the yellow arrows in (a) a typical region and (b) relatively rich region (Color figure online).

annealing for 1 hour. It appears that the Hf concentration has a correlation with the types and their sizes of the resultant phases. This suggests that it is possible to adjust the type and morphology of the formed phases by controlling the Hf content.

## IV. DISCUSSION

### A. Thermal Stability Mechanisms

The ferritic matrix of the Fe-14Cr-2Hf and Fe-14Cr-4Hf alloys retain nanocrystalline grain sizes after

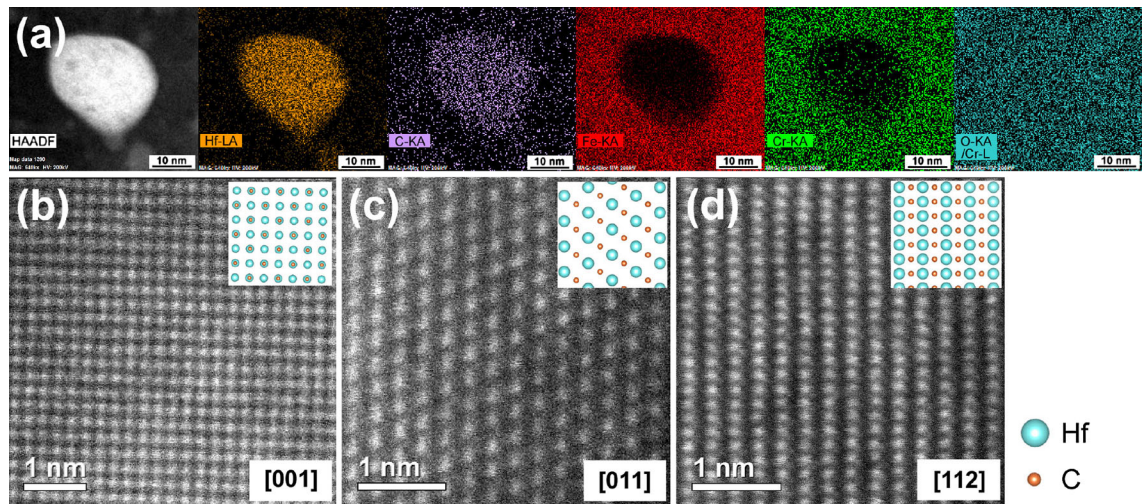


Fig. 7—EDS elemental mapping of the Hafnium Carbides. (a) HAADF-STEM image, and elemental mapping of Hf-L $\alpha$ , C-K $\alpha$ , Fe-K $\alpha$ , Cr-K $\alpha$ , and O-K $\alpha$ /Cr-L. (b) HAADF-STEM images of a hafnium carbide and the corresponding cartoon of lattice projection view along [001], (b) [011], and (c) [112] direction. The Hf atoms are shown as blue dots, and C atoms are shown as yellow dots. The STEM observation suggests a face-centered cubic structure of the phase which is consistent with the known hafnium carbide structure (Color figure online).

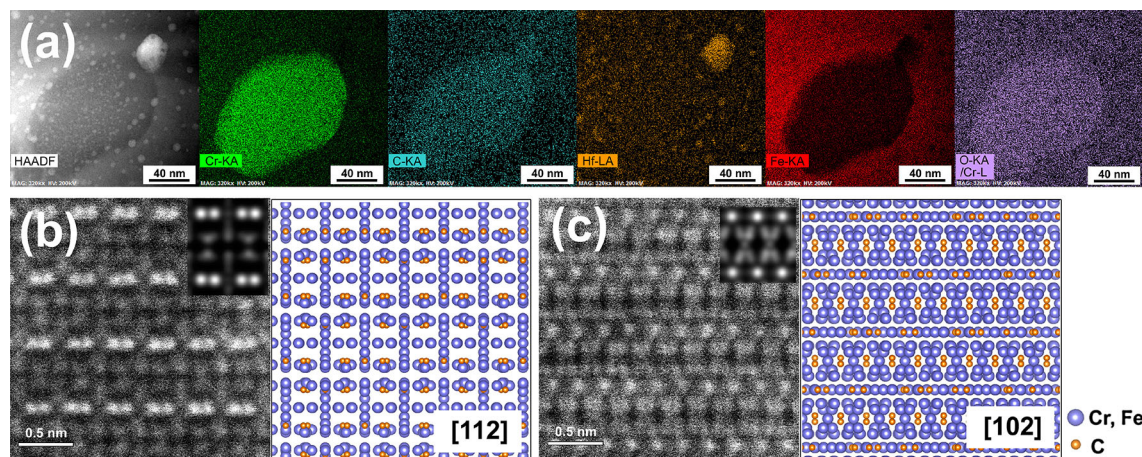


Fig. 8—EDS elemental mapping and high-resolution HAADF-STEM images of the  $M_{23}C_6$  phase. (a) HAADF-STEM image and EDS elemental mapping (Cr-K $\alpha$ , C-K $\alpha$ , Hf-L $\alpha$ , Fe-K $\alpha$ , and O-K $\alpha$ /Cr-L) of the  $M_{23}C_6$  phase. The atomic ratio of Cr to Fe within the carbide is determined to be 1:0.56 from the EDS data. The HAADF-STEM image, the simulated image (on the upper right corner of the HAADF-STEM image), and the cartoon of the lattice projection of the  $M_{23}C_6$  phase viewed along (b) [112] and (c) [102] direction. The Cr and Fe atoms are shown as purple dots, and C atoms are shown as yellow dots (Color figure online).

annealing at 1173 K (900 °C). This superior thermal stability is primarily attributed to the kinetic Zener pinning by dispersed HfO<sub>2</sub> nanoparticles. Figure 2(b) shows direct evidence of these particles pinning the grain boundaries, which helps with stabilizing the nanocrystalline matrix at elevated temperatures.

The critical grain size  $D_c$  due to particle pinning can be estimated using the Zener equation,<sup>[18]</sup>

$$D_c = K \frac{d}{f^m}, \quad [1]$$

where  $d$  and  $f$  are the average diameter and the volume fraction of the particles, respectively, and  $K$  and  $m$  are constants.

At low volume fractions ( $f < 5$  pct), the parameters  $K$  and  $m$  are taken to be 0.17 and 1, respectively, based on

empirical data.<sup>[18]</sup> In the case of the Fe-14Cr-2Hf alloy,  $f$  is estimated to be 1.19 pct from a region of 135 nm  $\times$  135 nm in area and 34 nm in thickness. By choosing the average HfO<sub>2</sub> particle size to be  $d = 3.9$  nm, the corresponding critical grain size  $D_c$  is around 58 nm, which is close to our observed value of 66 nm in Table I. Here, the HAADF-STEM image directly provides the total particle volume to calculate the  $f$  value due to the fact that it presents a projected image of all nanoparticles through the sample thickness. The sample thickness is measured by electron energy loss spectroscopy (EELS) using the log-ratio method.<sup>[51]</sup> For the Fe-14Cr-4Hf alloy, the value of  $f$  is estimated to be about 1.14 pct from a region of 135 nm  $\times$  135 nm  $\times$  37 nm. The estimated critical grain size  $D_c$  is 55 nm, which is also close to our experimental measurements of 57 nm in Table I.

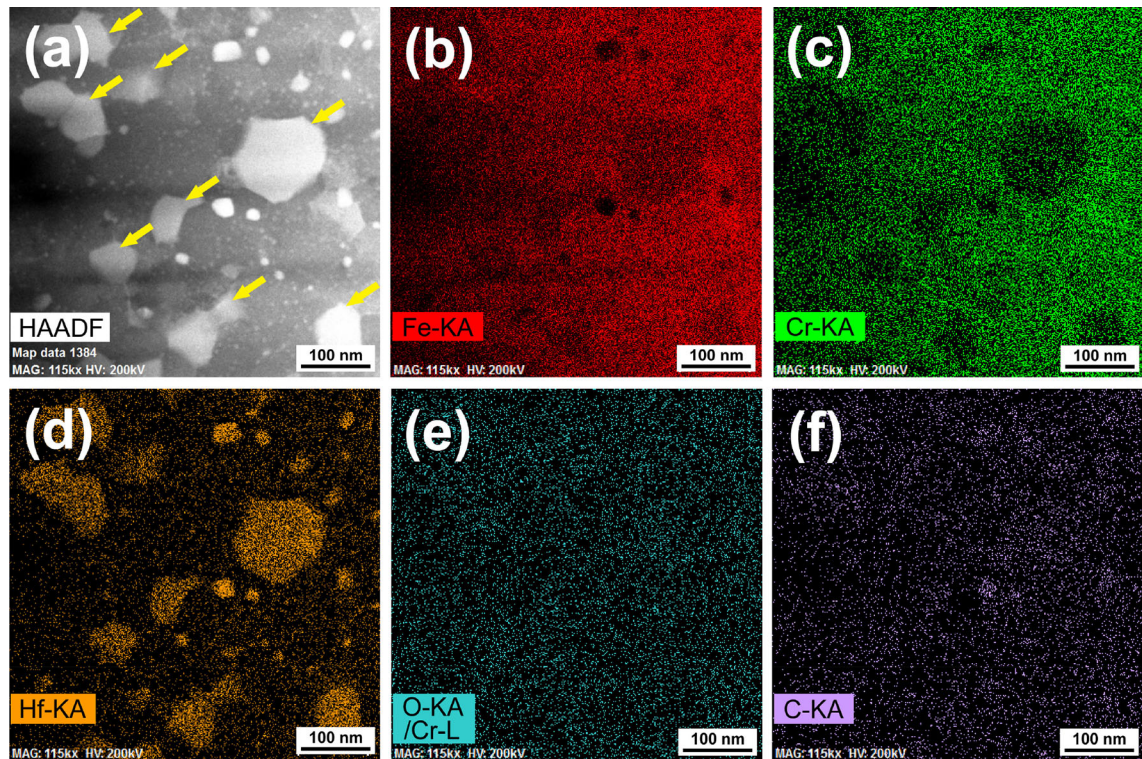


Fig. 9—EDS elemental mapping of a typical region of the Fe-14Cr-4Hf alloy (a) HAADF-STEM image and the elemental mapping of (b) Fe-K $\alpha$ , (c) Hf-L $\alpha$ , (d) Cr-K $\alpha$ , (e) C-K $\alpha$ , and (f) O-K $\alpha$ /Cr-L. The Fe-Cr-Hf intermetallic particles are pointed out by yellow arrows (Color figure online).

**Table I. Summary of the Existing Phases in the Fe-14Cr- $x$ Hf Alloys ( $x = 1, 2, 4$ ) and Their Sizes After Annealing at 1173 K (900 °C) for 1 h**

Phase\Alloy	Fe-14Cr-1Hf	Fe-14Cr-2Hf	Fe-14Cr-4Hf
Ferritic matrix	bimodal distribution 1 to 5 $\mu$ m and 100 to 300 nm	66 nm	57 nm
Hafnium oxide	4.3 nm	3.9 nm	3.7 nm
Hafnium carbide	Few/19 nm	23 nm	20 nm
M <sub>23</sub> C <sub>6</sub>	50 to 150 nm	not found	not found
Fe-Cr-Hf intermetallic	not found	not found	40 to 140 nm

The good agreement between the prediction from the Zener equation and our experimental measurements indicates that the superior thermal stability of the nanocrystalline Fe-14Cr-2Hf and Fe-14Cr-4Hf alloys can be primarily attributed to grain boundary pinning by dispersed nano-size HfO<sub>2</sub> particles. Note that other second-phase particles are also observed in the microstructure, such as hafnium carbide, M<sub>23</sub>C<sub>6</sub>, and Fe-Cr-Hf intermetallic. However, their particle inter-spacings are typically larger than the size of grains, making it impossible to cover the nanocrystalline grain boundary areas to produce the pinning effect. This means that the formation of nano-size and nano-spacing particles is essential for the stabilization of nanocrystalline structures. Similarly, nano-size ZrO<sub>2</sub> oxide particles were also found in a Fe-14Cr-1.5Zr alloy in a recent study,<sup>[22]</sup> in which high density of nano-size ZrO<sub>2</sub> particles significantly contributed to the thermal stability of the nanocrystalline grains. Such consistent results and mechanism in both Fe-14Cr- $x$ Hf and Fe-14Cr-1.5Zr alloys suggest the similar role of HfO<sub>2</sub> and ZrO<sub>2</sub>.

For the Fe-14Cr-1Hf alloy, the volume fraction  $f$  of the HfO<sub>2</sub> particles is estimated to be 0.86 pct from a 191 nm  $\times$  191 nm  $\times$  40 nm region. Using the Zener Eq. [1], the critical grain size of the matrix is predicted to be about 85 nm. This value is smaller than the 100 to 300 nm range, and much smaller than the 1 to 5  $\mu$ m range in the bimodal nano-micrograin size distribution observed in our experiments. Interestingly, both the ultrafine grains and the micron-size grains appear to contain a high density of HfO<sub>2</sub> particles with a similar particle size range and spatial density (see Figure 10). This indicates that the presence of HfO<sub>2</sub> did not stabilize the nanocrystalline grains in the Fe-14Cr-1Hf alloy.

The failure of HfO<sub>2</sub> in stabilizing the nanocrystalline grains in the Fe-14Cr-1Hf alloy is most likely because these HfO<sub>2</sub> particles did not precipitate fast enough to produce sufficient pinning force before grain boundaries moved to pass them.

Hf and O were supersaturated after the mechanical alloying process, which produced a non-equilibrium solid solution. During the annealing process at high



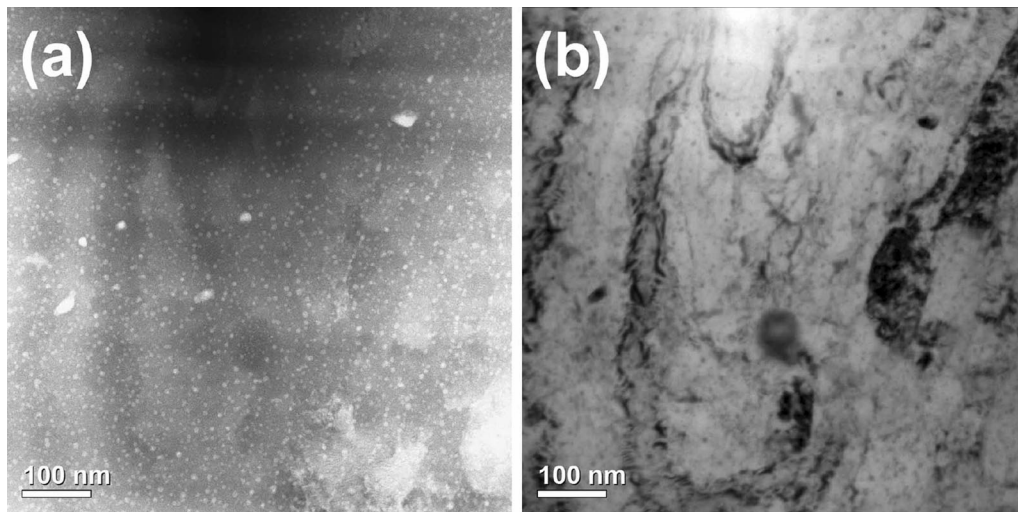


Fig. 10—Microstructure of the Fe-14Cr-1Hf alloy after annealing for 1 h at 1173 K (900 °C) containing both  $\mu\text{m}$  size and ultrafine grains. (a) HAADF-STEM images (b) Bright-field TEM images of the same area. High density of nano-size  $\text{HfO}_2$  particles are also observed in the  $\mu\text{m}$  size grain as well as in ultrafine grains.

temperatures,  $\text{HfO}_2$  particles precipitated out *via* a nucleation and growth process. Hf and O need to reach a critical concentration for the  $\text{HfO}_2$  nanoparticles to nucleate. Considering the much smaller Hf diffusion coefficient in iron ( $D_{\text{Hf}} = 1.60 \times 10^{-17} \text{ m}^2 \text{ s}^{-1}$ <sup>[52]</sup>) than that of the O atom ( $D_{\text{O}} = 3.01 \times 10^{-11} \text{ m}^2 \text{ s}^{-1}$ <sup>[53]</sup>) at 1173 K (900 °C) and similar O content in the Fe-14Cr- $x$ Hf alloys (as discussed in the Section IV-B), lower Hf content in the Fe-14Cr-1Hf alloy means longer diffusion time for Hf atoms to accumulate and also lower thermodynamic driving force for the nucleation of  $\text{HfO}_2$  nanoparticles. This will in principle result in longer incubation time for the nucleation of  $\text{HfO}_2$  nanoparticles. Moreover, the lower Hf solute concentration in the matrix also reduces the growth rate of the nucleated  $\text{HfO}_2$  particles, which could make it take longer time to achieve sufficient particle volume fraction for Zener pinning.<sup>[54]</sup>

The above discussion indicates a critical Hf content is needed to produce fast precipitation to ensure a good thermal stability at elevated temperatures. This is important for nanocrystalline alloys, because the precipitation is inevitably competing with high driving force for rapid grain growth at elevated temperatures. Such competition process between second-phase precipitation and the grain growth at the initial stage of annealing appears to be a critical factor in stabilizing nanocrystalline structure. In order to stabilize the nanocrystalline grain size, the pinning effect must be achieved fast enough before severe grain growth occurs.

In addition to that, the observed Hf and Cr grain boundary segregation in the high Hf concentration alloy (4 at. pct Hf) would further lower the driving force for grain growth to reduce the grain growth rate. This should have contributed to the additional thermodynamic stability in the Fe-14Cr-4Hf alloy as the model predicted.<sup>[27]</sup> Note that since such segregation seemed to occur only in high Hf content alloy and it only covered part of the grain boundaries, the effect of thermody-

amic stability due to the grain boundary segregation may not be significant in stabilizing nanocrystalline in Fe-14Cr- $x$ Hf alloys.

### B. The Presence of Oxygen and Carbon

Oxygen is not purposely added during mechanical alloying. However, 0.15 to 0.22 wt pct of oxygen is required in the Fe-14Cr- $x$ Hf alloy to form 0.8 to 1.2 pct volume fraction of the  $\text{HfO}_2$  particles. Oxygen should come from the as-received powders, since the particle sizes of pre-milled Fe and Cr powders are less than 10  $\mu\text{m}$ , which provides large surface area per volume for oxygen absorption during the storage.<sup>[55]</sup> Oxygen could also partially come from Hf powders, which contains 0.37 wt pct oxygen from the chemical composition analysis. The absorbed oxygen was then introduced into the ferritic matrix *via* mechanical alloying, forming  $\text{HfO}_2$  during subsequent annealing. The excess of oxygen is also found in our recent study of a Fe-14Cr-1.5Zr alloy.<sup>[22]</sup>

It is also found that carbides are formed in the alloys after annealing, which indicates that carbon also existed in the powder mixture. To form the carbides observed from the STEM, 0.1 to 0.2 wt pct carbon is required. This is much higher than the nominal carbon content in the as-received Fe, Cr, or Hf powders. The excessive carbon is most likely introduced by the milling media such as steel balls and vials during the mechanical alloying, since these milling media contain carbon concentration as high as 0.6 to 0.75 pct.

### C. The Precipitation of Second-Phases

As shown in Table I, different Hf concentrations in the alloy result in the formation of different types of precipitates after annealing at 1173 K (900 °C). Since the formation of precipitates will compete for solute atoms from the matrix, a clear understanding of the

second-phase precipitation behavior is fundamentally important.

The formation of different precipitates at different Hf concentrations can be understood by considering the Gibbs free energy of the phase formation. The Gibbs free energy for the formation of the  $\text{HfO}_2$  is  $\Delta G_f = -1263 \text{ kJ mol}^{-1}$ <sup>[56]</sup> at 1173 K (900 °C), which is much more negative than that for the formation of the hafnium carbide for which  $\Delta G_f = -221 \text{ kJ mol}^{-1}$  at 1173 K (900 °C).<sup>[57]</sup> The Gibbs free energy for the formation of the Fe-Cr-Hf intermetallic phase is expected to be around  $-100 \text{ kJ mol}^{-1}$ . This is based on the fact of Gibbs free energy for the  $\text{Zr}_2\text{Fe}$  ( $\Delta G_f = -105 \text{ kJ mol}^{-1}$ <sup>[50]</sup>) and the  $\text{Zr}_3\text{Fe}$  ( $\Delta G_f = -108 \text{ kJ mol}^{-1}$ <sup>[50]</sup>) at 1173 K (900 °C), and Hf and Zr compounds have very similar chemical properties.<sup>[33]</sup> The differences of the Gibbs free energy change for the phase formation suggest that there exists a preference for competing precipitation phases. Considering that  $\Delta G_f(\text{HfO}_2) < \Delta G_f(\text{HfC}) < \Delta G_f(\text{Fe-Cr-Hf})$ , the formation of the  $\text{HfO}_2$  phase is most favorable thermodynamically. Assuming that the formation kinetics for all phases are similar because they are all controlled by the slow diffusion of Hf,  $\text{HfO}_2$  is likely formed first because of its higher thermodynamic driving force. Consequently, the formation of  $\text{HfO}_2$  consumes the excess of Hf, which would suppress the formation of other Hf phases. This is consistent with the observed effect of the Hf content on the formation of certain phases in the Fe-14Cr-*x*Hf systems.

In an alloy with low Hf concentration, *e.g.*, Fe-14Cr-1Hf, Hf would be depleted due to the formation of  $\text{HfO}_2$ , thus suppressing the formation of the hafnium carbide and the Fe-Cr-Hf intermetallic phases. Therefore,  $\text{HfO}_2$  was observed as the primary precipitate phase in the Fe-14Cr-1Hf alloy (Figure 1(e)). In the case of higher Hf concentrations, *e.g.*, Fe-14Cr-4Hf, after the formation of  $\text{HfO}_2$  and HfC, there is still Hf left to form the Fe-Cr-Hf intermetallic phase and to segregate to grain boundaries. This explains why the Fe-Cr-Hf intermetallic phase and Hf segregation only formed in the 4 at. pct Hf alloy. This also indicates that the formation of  $\text{HfO}_2$  and HfC is more favorable than the Hf segregation to grain boundary.

Similarly, the co-existence of  $\text{M}_{23}\text{C}_6$  ( $(\text{Cr}_{0.64}\text{Fe}_{0.36})_{23}\text{C}_6$ ) with hafnium carbide is found in the Fe-14Cr-1Hf alloy, but not in the Fe-14Cr-2Hf or the Fe-14Cr-4Hf alloys. The Gibbs free energy for the formation of the  $\text{M}_{23}\text{C}_6$  is estimated to be around  $-70 \text{ kJ mol}^{-1}$  at 1173 K (900 °C),<sup>[58]</sup> which is less negative than that of hafnium carbide, which suggests that hafnium carbide is thermodynamically favored over  $\text{M}_{23}\text{C}_6$ . In an alloy with relatively high Hf concentration, *e.g.*, Fe-14Cr-2Hf or Fe-14Cr-4Hf, hafnium oxide will form first, followed by hafnium carbide. The excess hafnium would deplete carbon to form the HfC phase, leaving little carbon to form the  $\text{M}_{23}\text{C}_6$  phase. In contrast, in the Fe-14Cr-1Hf alloy, the low concentration of Hf is depleted to form the  $\text{HfO}_2$ , leaving small amount of Hf to form HfC. As a result, some carbon will be left to form the  $\text{M}_{23}\text{C}_6$  phase, where  $\text{M} = \text{Fe, Cr}$ .

## V. SUMMARY

In summary, we present a comprehensive microstructural analysis for the nanocrystalline Fe-14Cr-*x*Hf alloys ( $x = 1, 2, \text{ and } 4 \text{ at. pct}$ ) after annealing at 1173 K (900 °C) for 1 hour. The Fe-14Cr-1Hf alloy shows a bimodal grain size distribution with 100 to 300 nm fine grains and 1 to 5  $\mu\text{m}$  coarse grains. The Fe-14Cr-2Hf and Fe-14Cr-4Hf alloys show excellent thermal stability and retain nanocrystalline structure with average grain sizes of about 66 and 56 nm, respectively.

High density of  $\text{HfO}_2$  particles with an orthorhombic crystal structure and sizes of  $\sim 4 \text{ nm}$  are observed in all three Fe-14Cr-*x*Hf alloys. These nano-size particles are dispersed throughout the ferritic matrix, which provides effective kinetic pinning to stabilize nanocrystalline structure. The bi-modal grain structure in the Fe-14Cr-1Hf alloy is attributed to the slow formation of  $\text{HfO}_2$  particle due to low Hf supersaturation during the annealing. Hf and Cr are also found co-segregated at some grain boundaries in the Fe-14Cr-4Hf alloy, providing some limited additional thermodynamic stabilization.

Hafnium carbide,  $\text{M}_{23}\text{C}_6$ , and Fe-Cr-Hf intermetallic phase are also found in the alloys. EDS analysis shows the chemical composition of  $\text{M}_{23}\text{C}_6$  to be  $(\text{Cr}_{0.64}\text{Fe}_{0.36})_{23}\text{C}_6$ . The atomic ratio of the Fe to Cr to Hf is 1:0.08:0.33 in the Fe-Cr-Hf intermetallic phase.

The Gibbs free energies for the formation of different phases at 1173 K (900 °C) are estimated as  $\Delta G_{f,\text{HfO}_2} (-1263 \text{ kJ mol}^{-1}) < \Delta G_{f,\text{HfC}} (-221 \text{ kJ mol}^{-1}) < \Delta G_{f,\text{Fe-Cr-Hf}} (-100 \text{ kJ mol}^{-1}) < \Delta G_{f,\text{M}_{23}\text{C}_6} (\sim -70 \text{ kJ mol}^{-1} \text{ per C})$ , which largely determines the formation sequence of these phases. Precipitation of different phases is found to depend on Hf concentration. In the Fe-14Cr-1Hf alloy,  $\text{HfO}_2$ , small amount of hafnium carbide, and  $\text{M}_{23}\text{C}_6$  are found.  $\text{HfO}_2$  and hafnium carbide are formed in the Fe-14Cr-2Hf alloy, while  $\text{HfO}_2$ , hafnium carbide, and Fe-Cr-Hf intermetallic phase are formed in the Fe-14Cr-4Hf alloy.

## ACKNOWLEDGMENTS

We acknowledge financial support from the Department of Energy Idaho Field Office (DEN0000538). The authors also acknowledge the use of the Analytical Instrumentation Facility (AIF) at North Carolina State University, which was supported by the State of North Carolina and the National Science Foundation.

## ELECTRONIC SUPPLEMENTARY MATERIAL

The online version of this article (doi: [10.1007/s11661-015-2985-2](https://doi.org/10.1007/s11661-015-2985-2)) contains supplementary material, which is available to authorized users.

## REFERENCES

1. C. Suryanarayana: *Int. Mater. Rev.*, 1995, vol. 40, pp. 41–64.
2. H. Gleiter: *Acta Mater.*, 2000, vol. 48, pp. 1–29.
3. L. Lu, M.L. Sui, and K. Lu: *Science*, 2000, vol. 287, pp. 1463–66.
4. Y.T. Zhu, T.C. Lowe, and T.G. Langdon: *Scripta Mater.*, 2004, vol. 51, pp. 825–30.
5. M.A. Meyers, A. Mishra, and D.J. Benson: *Prog. Mater. Sci.*, 2006, vol. 51, pp. 427–556.
6. C. Koch: *J. Mater. Sci.*, 2007, vol. 42, pp. 1403–14.
7. V.Y. Gertsman and R. Birringer: *Scripta Metal. et Mater*, 1994, vol. 30, pp. 577–81.
8. J.A. Haber and W.E. Buhro: *J. Am. Chem. Soc.*, 1998, vol. 120, pp. 10847–55.
9. K. Hansen and K. Pantleon: *Scripta Mater.*, 2008, vol. 58, pp. 96–98.
10. M. Saber, H. Kotan, C.C. Koch, and R.O. Scattergood: *Mater. Sci. Eng. A*, 2012, vol. 556, pp. 664–70.
11. K.A. Darling, B.K. VanLeeuwen, C.C. Koch, and R.O. Scattergood: *Mater. Sci. Eng. A*, 2010, vol. 527, pp. 3572–80.
12. K.A. Darling, R.N. Chan, P.Z. Wong, J.E. Semones, R.O. Scattergood, and C.C. Koch: *Scripta Mater.*, 2008, vol. 59, pp. 530–33.
13. R.A. Andrievski: *J. Mater. Sci.*, 2014, vol. 49, pp. 1449–60.
14. Y. Chen, Y. Liu, F. Khatkhatay, C. Sun, H. Wang, and X. Zhang: *Scripta Mater.*, 2012, vol. 67, pp. 177–80.
15. B. Huang, R.J. Perez, and E.J. Lavernia: *Mater. Sci. Eng. A*, 1998, vol. 255, pp. 124–32.
16. K. Maung, R.K. Mishra, I. Roy, L.C. Lai, F.A. Mohamed, and J.C. Earthman: *J. Mater. Sci.*, 2011, vol. 46, pp. 6932–40.
17. G.D. Hibbard, K.T. Aust, and U. Erb: *Mater. Sci. Eng. A*, 2006, vol. 433, pp. 195–202.
18. P.A. Manohar, M. Ferry, and T. Chandra: *ISIJ Int.*, 1998, vol. 38, pp. 913–24.
19. H.A. Murdoch and C.A. Schuh: *Acta Mater.*, 2013, vol. 61, pp. 2121–32.
20. T. Chookajorn, H.A. Murdoch, and C.A. Schuh: *Science*, 2012, vol. 337, pp. 951–54.
21. M. Saber, H. Kotan, C.C. Koch, and R.O. Scattergood: *J. Appl. Phys.*, 2013, vol. 113, p. 063515.
22. W. Xu, L. Li, M. Saber, C.C. Koch, Y. Zhu, and R.O. Scattergood: *J. Nucl. Mater.*, 2014, vol. 452, pp. 434–39.
23. A.A. Talin, E.A. Marquis, S.H. Goods, J.J. Kelly, and M.K. Miller: *Acta Mater.*, 2006, vol. 54, pp. 1935–47.
24. M. da Silva, C. Wille, U. Klement, P. Choi, and T. Al-Kassab: *Mater. Sci. Eng. A*, 2007, vols. 445–446, pp. 31–39.
25. T. Hentschel, D. Isheim, R. Kirchheim, F. Müller, and H. Kreye: *Acta Mater.*, 2000, vol. 48, pp. 933–41.
26. S.C. Mehta, D.A. Smith, and U. Erb: *Mater. Sci. Eng. A*, 1995, vol. 204, pp. 227–32.
27. L. Li, M. Saber, W. Xu, Y. Zhu, C.C. Koch, and R.O. Scattergood: *Mater. Sci. Eng. A*, 2014, vol. 613, pp. 289–95.
28. N. Zhou and J. Luo: *Mater. Lett.*, 2014, vol. 115, pp. 268–71.
29. T.F. Kelly and M.K. Miller: *Rev. Sci. Instrum.*, 2007, vol. 78, p. 031101.
30. C.M. Parish, R.M. White, J.M. LeBeau, and M.K. Miller: *J. Nucl. Mater.*, 2014, vol. 445, pp. 251–60.
31. D.E. Jesson and S.J. Pennycook: *Proc. R. Soc. Lond. A: Math. Phys. Sci.*, 1995, vol. 449, pp. 273–93.
32. HSV Harrach, P. Dona, B. Freitag, H. Soltau, A. Niculae, and M. Rohde: *J. Phys.: Conf. Series*, 2010, vol. 241, p. 012015.
33. J. Wang, H.P. Li, and R. Stevens: *J. Mater. Sci.*, 1992, vol. 27, pp. 5397–30.
34. C.T. Koch: Ph.D. Thesis, Arizona State University, 2002.
35. P.A. Stadelmann, (JEMS—EMS java version: 2010).
36. O. Ohtaka, T. Yamanaka, S. Kume, N. Hara, H. Asano, and F. Izumi: *J. Am. Ceram. Soc.*, 1995, vol. 78, pp. 233–37.
37. C.E. Curtis, L.M. Doney, and J.R. Johnson: *J. Am. Ceram. Soc.*, 1954, vol. 37, pp. 458–65.
38. RE Hann, PR Suitch, and JL Pentecost: *J. Am. Ceram. Soc.*, 1985, vol. 68, pp. C-285–286.
39. O. Ohtaka, H. Fukui, T. Kunisada, T. Fujisawa, K. Funakoshi, W. Utsumi, T. Irifune, K. Kuroda, and T. Kikegawa: *J. Am. Ceram. Soc.*, 2001, vol. 84, pp. 1369–73.
40. G. Skandan, C.M. Foster, H. Frase, M.N. Ali, J.C. Parker, and H. Hahn: *Nanostruct. Mater.*, 1992, vol. 1, pp. 313–22.
41. A. Suresh, M.J. Mayo, W.D. Porter, and C.J. Rawn: *J. Am. Ceram. Soc.*, 2003, vol. 86, pp. 360–62.
42. J.E. Daniels, M.V. Manuel, C.W. Brink, and J.L. Jones: *Scripta Mater.*, 2009, vol. 61, pp. 391–94.
43. R.C. Garvie and M.V. Swain: *J. Mater. Sci.*, 1985, vol. 20, pp. 1193–200.
44. J.H. Choi, Y. Mao, and J.P. Chang: *Mater. Sci. Eng. R*, 2011, vol. 72, pp. 97–136.
45. H. Okamoto: *Bull. Alloy Phase Diagr.*, 1990, vol. 11, pp. 396–403.
46. A.L. Bowman, G.P. Arnold, E.K. Storms, and N.G. Nereson: *Acta Crystallog. B*, 1972, vol. 28, pp. 3102–03.
47. B. Predel: *Fe-Hf (Iron-Hafnium)*, SpringerMaterials—The Landolt-Börnstein Database, Springer, Berlin, 1996.
48. M. Venkatraman and J.P. Neumann: *Bull. Alloy Phase Diagr.*, 1986, vol. 7, pp. 570–73.
49. Y. Liu, S.M. Allen, and J.D. Livingston: *Scripta Metall. et Mater.*, 1995, vol. 32, pp. 1129–32.
50. A.D. Pelton, L. Leibowitz, and R.A. Blomquist: *J. Nucl. Mater.*, 1993, vol. 201, pp. 218–24.
51. T. Malis, S.C. Cheng, and R.F. Egerton: *J. Electron Microsc. Technol.*, 1988, vol. 8, pp. 193–200.
52. A.W. Bowen and G.M. Leak: *Metall. Trans.*, 1970, vol. 1, pp. 1695–700.
53. J. Takada and M. Adachi: *J. Mater. Sci.*, 1986, vol. 21, pp. 2133–37.
54. C. Wert and C. Zener: *J. Appl. Phys.*, 1950, vol. 21, pp. 5–8.
55. Z. Oksiuta and N. Baluc: *Nucl. Fusion*, 2009, vol. 49, p. 055003.
56. M.C. Zeman, C.C. Fulton, G. Lucovsky, R.J. Nemanich, and W.C. Yang: *J. Appl. Phys.*, 2006, vol. 99, p. 023519.
57. Y. Ye, H. Zhang, Y. Tong, and S. Bai: *Ceram. Inter.*, 2013, vol. 39, pp. 5477–83.
58. S. Shatynski: *Oxid. Met.*, 1979, vol. 13, pp. 105–18.